Structure and Electrochemical Properties of Boron-Doped LiCoO$_2$

R. Alcántara, P. Lavela, and J. L. Tirado[1]

Laboratorio de Química Inorgánica, Facultad de Ciencias, Universidad de Córdoba, Avda. San Alberto Magno s/n, 14004 Córdoba, Spain

and

R. Stoyanova and E. Zhecheva

Institute of General and Inorganic Chemistry, Bulgarian Academy of Sciences, 1113 Sofia, Bulgaria

XRD, ^{6}Li and ^{11}B MAS NMR, IR, and EPR of low-spin Ni^{3+} probes were used for the structural characterization of boron-doped LiCoO$_2$. Up to 5 atom % boron additives were shown to dissolve in trigonal LiCoO$_2$. The structure of the CoO$_2$ sandwiches remained unaffected by this treatment. The boron environment was assessed by spectroscopic analysis, which showed a distorted tetrahedral coordination. The boron-doped LiCoO$_2$ samples were used as active electrode materials in lithium cells. Step potential electrochemical spectroscopy and galvanostatic cycling revealed that boron dopants improve the reversibility of the lithium deintercalation–intercalation process and favor lattice adaptation to lithium order–disorder in the depleted LiO$_2$ layers. © 1997 Academic Press

INTRODUCTION

Rechargeable lithium-ion batteries using a transition metal oxide (Li$_x$MO$_2$, M = first-row transition metal) as an intercalation compound for the positive electrode have gained popularity during the past 5 years. LiCoO$_2$ is now considered a reference compound as a result of being the active cathode material in the first commercial lithium-ion product. This solid possesses practically the idealized α-NaFeO$_2$ type structure where distinct layers of Li and Co alternate in the six-coordinated sites defined by a cubic close packing of oxygen atoms (1, 2). These features put LiCoO$_2$ in a more advanced position as compared to LiNiO$_2$ and LiMn$_2$O$_4$ with respect to their utilization as cathode materials in 4-V lithium secondary batteries (3, 5).

For secondary lithium batteries based on lithium transition metal oxides, the main operating problems arise from the capacity drop resulting from irreversible structural and morphological changes in the composite electrode during consecutive charge–discharge cycles. An effective way to improve the rechargeability of the cathode material is to make its structure more flexible. Following the materials chemistry rules, the structural modification of solids can be achieved by doping and/or by changing the preparation conditions. For LiCoO$_2$, it has been shown that doping with nickel, having an ionic radius close to that of Co^{3+}, improves its cycleability (6–9) but manganese and chromium additives, which have larger ionic radii, deteriorate the electrochemical performance (10, 11). In the patent literature, there are some data on the use of new cathode materials based on LiCoO$_2$ with W, Ta, Ti, Nb, and B additives (12, 13). Thus, it was established that batteries using B-doped LiCoO$_2$ as active cathode material have improved charge–discharge cycle performance and long life (13).

Concerning the effect of the preparation conditions on the structural modification, low- and high-temperature synthesis techniques yield LiCoO$_2$ with different crystal structures and specific surface areas: LT-LiCoO$_2$ with $S \cong$ 15–20 m^2/g has a pseudospinel structure with $c/a = 4.90$ (space group $Fd\bar{3}m$) (14–16), whereas HT-LiCoO$_2$ with $S \leq 1$ m^2/g displays a layered structure with $c/a > 4.97$ (space group $R\bar{3}m$) (2). However, the electrochemical behavior of LT-LiCoO$_2$ (initial capacity and cycle life) is much worse as compared to the high-temperature layered analog (9, 16, 17).

In the present paper, we report data on the structural modification of LiCoO$_2$ induced by doping with boron. In addition, the electrochemical performance of B-doped LiCoO$_2$ in lithium cells is studied.

EXPERIMENTAL

The B-doped samples were prepared by the solid-state reaction between LiOH · H$_2$O, Co$_3$O$_4$ (from cobalt hydroxide–carbonate containing ca. 0.4 at.% Ni), and H$_3$BO$_3$. The

---

[1] To whom correspondence should be addressed.

mixture of the initial compounds, taken in appropriate amounts (Li : Co : B = 1 : (1 − x) : x; 0 ≤ x ≤ 0.2), was homogenized and treated thermally as follows: 4 h at 170°C (temperature of dehydration to metaboric acid), 24 h at 450°C (melting point of LiOH), and, finally, 24 h at 800°C, with an intermediate grinding between the different temperature steps.

The lithium content of the samples was determined by atomic absorption analysis. The total amount and the mean oxidation state of Co were determined by complexometric and iodometric titration, respectively.

The X-ray phase analysis was performed with a Philips diffractometer using $CuK\alpha$ radiation. The infrared spectra were recorded with a Specord-75 (ex-GDR) spectrometer in KBr tablets.

^{6}Li and ^{11}B MAS NMR spectra were obtained with a Bruker ACP-400 apparatus working at 58.89- and 128.39-MHz resonance frequencies, respectively (9.400 T) and at a 5-kHz spinning rate.

The EPR spectra were registered as the first derivative of the absorption signal with an ERS-220/Q spectrometer (ex-GDR) within the temperature range 90–400 K. The g factors were established with respect to a Mn^{2+}/ZnS standard. The signal intensity was determined by double integration of the experimental EPR spectrum.

Scanning electron microscopy (SEM) measurements were carried out with a JEOL 5300 instrument with 15- and 25-kV accelerating voltage.

Electrochemical measurements of $LiCoO_2$-B samples were performed in two-electrode cells by using 1 M $LiClO_4$ in EC : PC (ethylene carbonate : propylene carbonate) = 1 : 1 as the electrolyte and lithium foil as the anode. The cathode pellets (7-mm diameter) containing ca. 10 mg of the active electrode oxide sample were prepared by dispersing a mixture of 80% oxide, 12% carbon black (Strem 4N), and 8% EPDM in cyclohexane. The solvent was evaporated at room temperature and the slurry was completely dried, powdered, and compressed at 3.5 Tm. All electrochemical measurements were carried out with a MacPile multichannel system. Step potential electrochemical spectroscopy (SPES) was carried out with 10 mV/h steps after an initial relaxation of the cell until the condition $\Delta V/\Delta t < 1$ mV/h. Galvanostatic cycling was performed in the as-prepared cells at $C/100$ (i.e., allowing a $\Delta x = 1$ in Li_xCoO_2 in 100 h).

RESULTS AND DISCUSSION

Doping of $LiCoO_2$ with B does not change its layered structure: the X-ray diffraction (XRD) patterns consist only of diffraction lines of a trigonally distorted NaCl structure (space group $R\bar{3}m$). The unit cell parameters (a and c) for pure $LiCoO_2$ and B-doped samples are compared in Table 1. If a low extent of substitution of larger cobalt ions by boron is present, the unit cell should tend to contract. On

TABLE 1
Unit Cell Parameters ($a \pm 0.003$ Å and $c \pm 0.02$ Å) for the $R\bar{3}m$ Space Group and c/a Ratio for B-Doped $LiCoO_2$

B/(B + Co)	a (Å)	c (Å)	c/a
0.00	2.817	13.99	4.97
0.05	2.810	13.96	4.97
0.10	2.812	13.97	4.97
0.20	2.806	13.93	4.97

the contrary, if the B atoms are located in crystallographic sites different from those used by the constituent atoms in stoichiometric $LiCoO_2$, a reduction in cell volume may not occur. The latter possibility is in agreement with the values shown in Table 1, as no clear decreasing sequence in the unit cell parameters is found and the variations fall within the limits of the experimental errors. Moreover, the degree of trigonal distortion of the cubic lattice (expressed by the c/a ratio) remained basically unchanged during doping with B (Table 1). Attempts to apply the Rietveld method of profile fitting to the XRD data (Fig. 1) were carried out by first assuming that boron substitutes isomorphically for Co in the $3a$ pseudooctahedral ($\bar{3}m$) sites of the CoO_2 layers (Fig. 2). Due to the low scattering power of B atoms as compared with cobalt, small amounts of B replacing Co in the CoO_2 layers should lead to significant changes in the intensity of the diffraction lines affected by the scatterers located in $3a$ sites. However, the Bragg R_B factors obtained by using this model took values of ca. 16% and the ratio R_{wp}/R_{exp} was always higher than 2. These results are indicative of a poor fitting of both the integrated intensities and the complete pattern, due to an inappropriate description of site occupancy in B-doped samples. Thus the results can be interpreted as conclusive evidence of the absence of B atoms replacing Co. The evaluation of an alternative model in which Co site occupancy is not affected by the presence of boron is limited by the low scattering power of B atoms and their low proportion. Thus the exact location of these atoms is uncertain by X-ray diffraction. Nevertheless, a pseudo-tetrahedral ($3m$) site occupancy for B in CoO_2 layers ($6c$ sites with $z_B > z_O$) (Fig. 2) can be considered reasonable on account of the preference of boron for low coordination number (3 and 4). A better Rietveld fitting was observed in this case, with R_B values lower than 10% and R_{wp}/R_{exp} close to unity (Fig. 1). However, these results should be interpreted with caution and the identification of the sites occupied by boron must be assessed by the spectroscopic results discussed below.

Figure 3 presents SEM pictures of $LiCoO_2$ and $LiCoO_2$-B. Well-crystallized platelike particles are observed for both types of samples, with a relatively broad crystal size distribution. However, a significant growth of the crystallite size is observed for the B-doped samples: the diameter of the
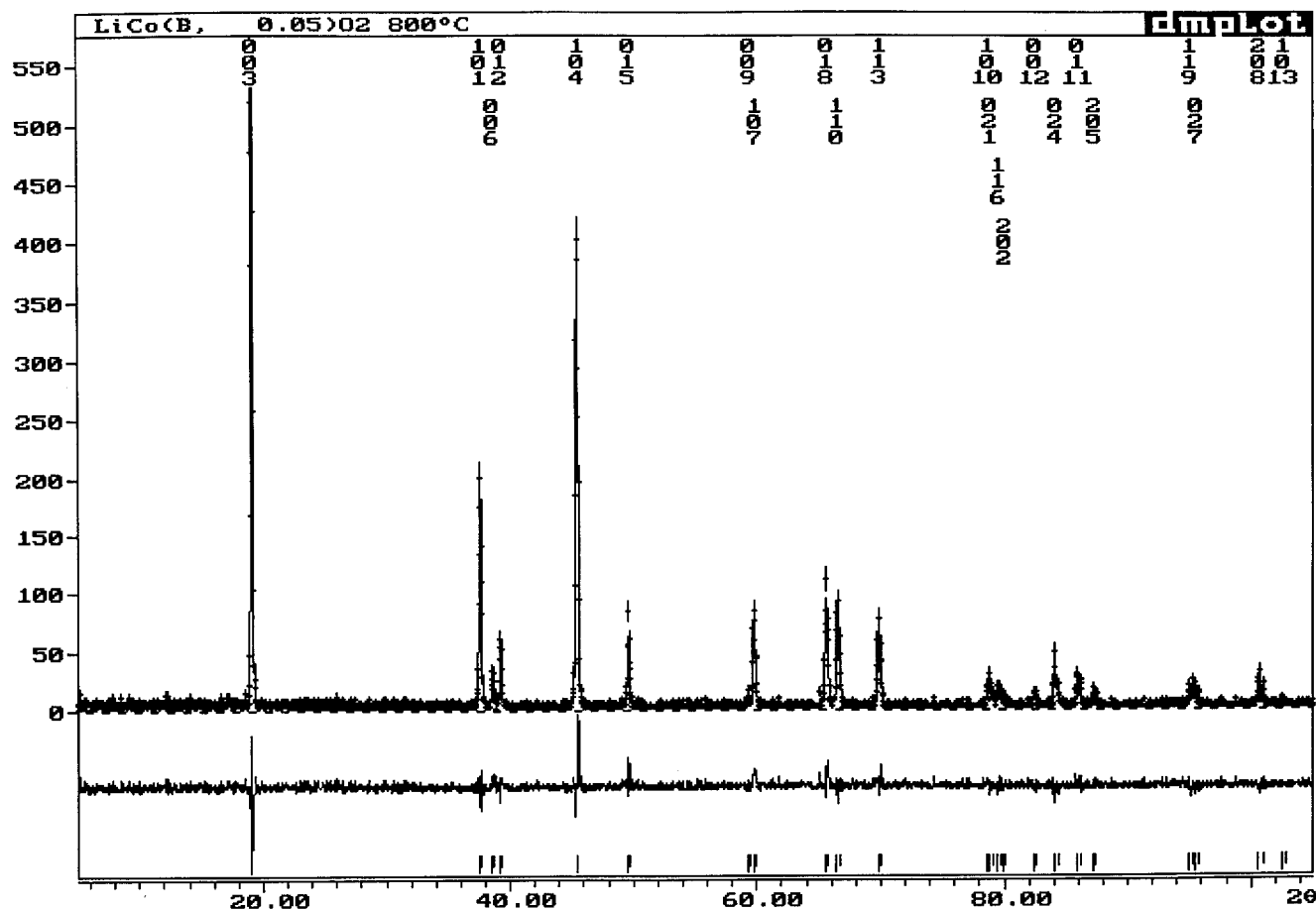
FIG 1. Results of the Rietveld profile fitting of the 5% B-doped LiCoO$_2$ sample, using an $R\bar{3}m$ model with Co in $3a$, Li in $3b$, O in $6c$ ($z_O = 0.259$), and B in $6c$ ($z_B = 0.295$).

particles varies between 0.5 and 3 μm for pure LiCoO$_2$ and between 1.5 and 6 μm for B-doped LiCoO$_2$.

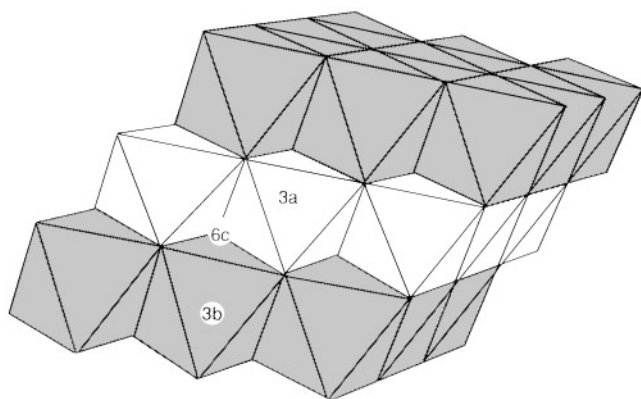The incorporation of boron into the LiCoO$_2$ lattice can be followed in the IR spectra of the oxides. According to the theoretical group analysis, the number of IR-active modes is four (18, 19). For LiMO$_2$ oxides, the vibrations of the LiO$_2$ and CoO$_2$ layers are separated (two-mode behavior), so that the number of the predicted bands is doubled: at 400–700 cm^{-1} there are bands due to CoO$_2$ vibrations, whereas the LiO$_2$ vibrations are within the region 200–400 cm^{-1} (18, 19). As is evident from Fig. 4, four bands can be resolved in the IR spectrum of LiCoO$_2$ in the region 400–700 cm^{-1}: three intense bands at 646, 598, and 538 cm^{-1} and one weak band at 554 cm^{-1}. Small amounts of boron additives in LiCoO$_2$ shift the positions of the first two intensive bands in opposite directions: the 646-cm^{-1} band is shifted to higher wavenumbers and the 598-cm^{-1} band is shifted to lower wavenumbers (Fig. 4). The boron-induced changes in CoO$_2$ vibrations show that B additives reside mainly in the CoO$_2$ slabs. In addition, weak bands at 1430, 1145, 740, and 724 cm^{-1} grow in the IR spectra of the samples with a high B content ($x \geq 0.1$). According to IR investigations on borate glasses (20, 21), these bands correspond to the vibrational modes of the pyroborate group (B$_2$O$_5$) and/or the metaborate group (BO$_3$): B–O bond

FIG 2. Schematic representation of LiO$_2$ and CoO$_2$ layers (shaded and empty octahedra, respectively).
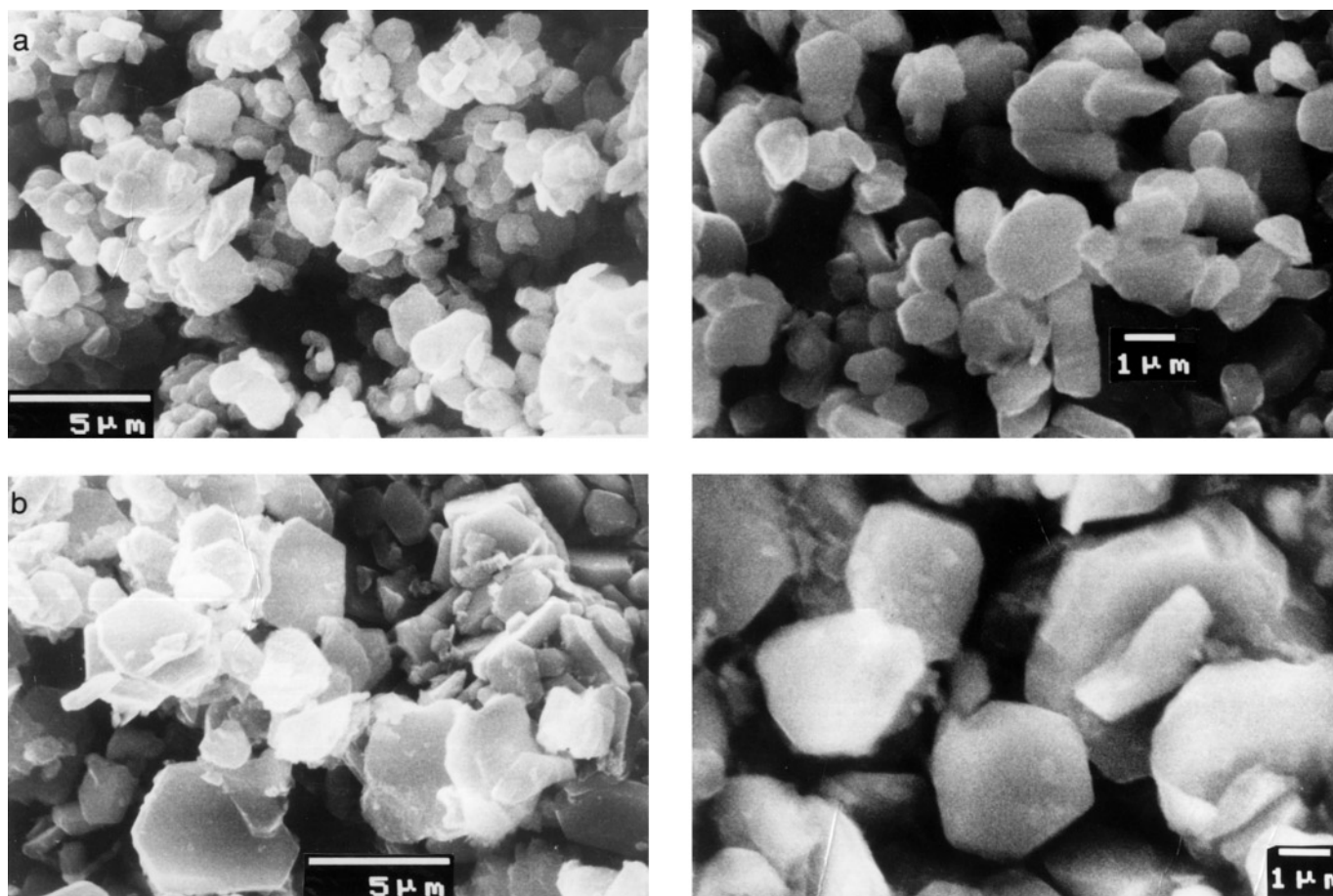
FIG 3. SEM micrographs of pure LiCoO$_2$ (a) and LiCoO$_2$ doped with 10 atom % boron (b).

stretching vibrations (1430 cm^{-1}), B–O–B asymmetric stretching vibrations (1145 cm^{-1}), and B–O–B bond bending vibrations (740 and 724 cm^{-1}). Taking into account the high reactivity of Li$_2$O toward B$_2$O$_3$, this result suggests that for the samples with a higher B content an impurity phase of lithium pyroborate/metaborate also appears.

The effect of B on the lattice dynamics of LiCoO$_2$ can be indirectly monitored by EPR. Pure LiCoO$_2$ is diamagnetic, but usually Co salts contain Ni impurities ($< 0.4\%$) which can be used as EPR probes in LiCoO$_2$ (22). Impurity Ni^{3+} ions occupy two crystal sites of LiCoO$_2$: most of the Ni^{3+} ions substitute isomorphically for Co^{3+} in the CoO$_2$ layers (trigonally distorted octahedra), but some of the Ni^{3+} ions are in tetragonally elongated octahedra related to some defects (surfaces) of the matrices (22). At temperatures higher than 210 K, the EPR spectrum of low-spin Ni^{3+} exhibits a typical dynamic Jahn–Teller behavior for a system with an ^{2}E ground state: a single Lorentzian with $g = 2.142$ is observed and the EPR line width is narrowed with increasing registration temperature (22). Between 150 and 210 K, the EPR line width reaches its minimum value,

which depends on the Ni^{3+} concentration in the LiCoO$_2$ matrix (22). Data on the temperature-independent line width (ΔH_{pp}°) for LiCoO$_2$ and LiCoO$_2$-B samples are summarized in Table 2. It can be seen that ΔH_{pp}° increases with rising B content. At temperatures above 210 K, the EPR line widths are broadened for all samples due to spin–lattice relaxation processes (Fig. 5). In this temperature region, the experimental dependence of ΔH_{pp} on registration temperature is fitted best with a quadratic function:

$$\Delta H_{pp} = \Delta H_{pp}^\circ + b\,T^2, \quad T > 210 \text{ K} \qquad [1]$$

This "T^2 function" indicates that Ni^{3+} ions relax independently by Raman interactions with the phonon reservoir. The values of $d(\Delta H_{pp} - \Delta H_{pp}^\circ)/dT^2$ for the different samples (which are reciprocal to the spin–lattice relaxation time) are also presented in Table 2. Doping of LiCoO$_2$ with small amounts of B (5 atom %) sharply increases the spin–lattice relaxation time of the impurity Ni^{3+} ions. In addition, higher B concentrations do not affect the relaxation processes. The longer spin–lattice relaxation time of
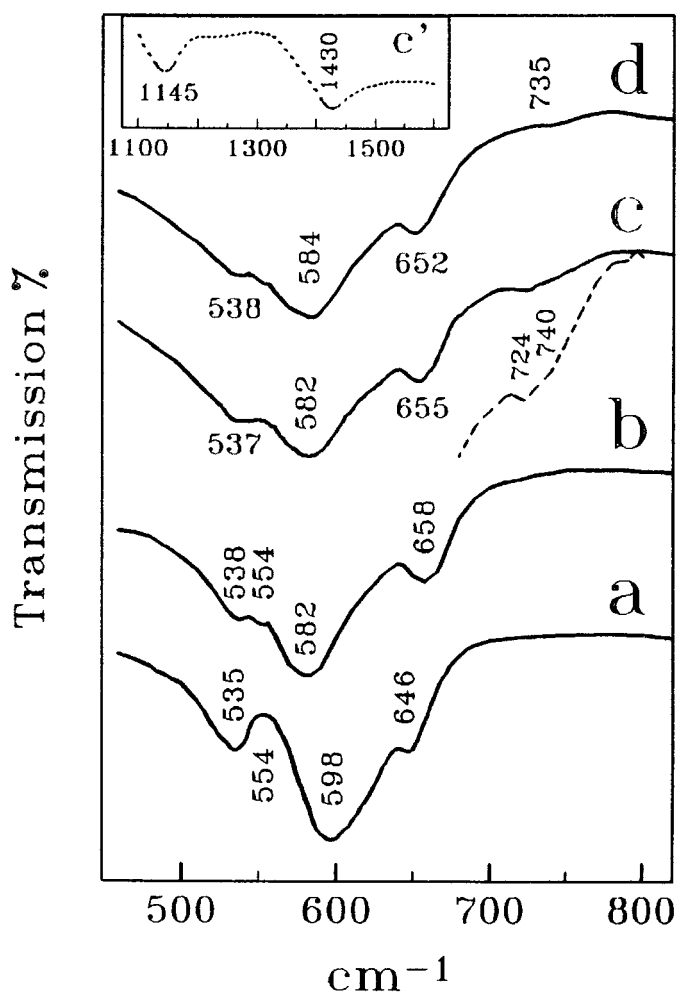
FIG 4. IR spectra of pure $LiCoO_2$ (a) and B-doped $LiCoO_2$: 5 (b), 10 (c), and 20 atom % (d). The spectra represented by broken lines correspond to more concentrated KBr pellets.
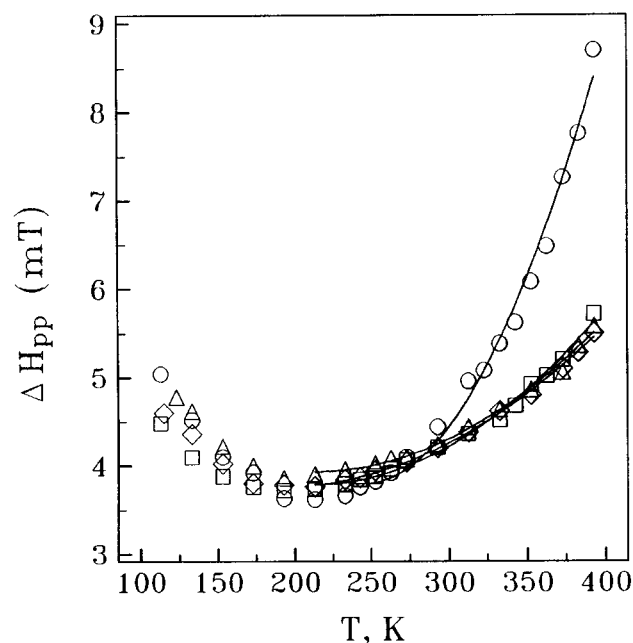

FIG 5. Temperature dependence of the EPR line width of pure $LiCoO_2$ (z) and B-doped $LiCoO_2$: 5 (□), 10 (◇), and 20 (△).

impurity Ni^{3+} ions in B-doped samples is a proof for changes in crystal lattice dynamics, which is in accordance with IR data (Fig. 4). In addition, for the B-doped samples the intensity of the EPR signal, which is proportional to the Ni^{3+} amount, increases (Table 2). This means that B dopant atoms enhance the Ni^{3+} solubility in the $LiCoO_2$ matrix.

TABLE 2
Temperature-Independent EPR Line Width (ΔH_{pp}°, mT), $d(\Delta H_{pp} - \Delta H_{pp}^{\circ})/dT^2$ Coefficient ($b \pm 0.10$ mT/K²), and EPR Signal Intensity ($I \pm 0.2$, au) for B-Doped $LiCoO_2$

B/(B + Co)	ΔH_{pp}°	$b \times 10^{-5}$	I
0.00	3.36	4.52	1.0
0.05	3.70	1.87	5.1
0.10	3.86	1.69	3.4
0.20	3.80	1.71	3.0

(We must recollect that the Ni^{3+} amount is much lower than that of B^{3+}: Ni ≤ 0.4 at.% and B ≥ 5 at.%.) The increased amount of Ni^{3+} in B-doped $LiCoO_2$ may explain the broadening of the temperature-independent EPR line width (Table 2). For a statistical distribution, the dipole–dipole spin interactions induce a quadratic dependence of the EPR line width on the spin amount: $\Delta H_{pp}^2 = \text{const} \times c$ (23). However, the theoretical dependence is not obeyed in B-doped samples, thus indicating nonuniform distribution of impurity Ni^{3+} ions in the CoO_2 slabs. This result is not surprising, taking into account the great difference in the ionic radii of B^{3+}, Co^{3+}, and Ni^{3+} ions for a coordination number of 6: $r_B = 0.27$ Å, $r_{Co(LS)} = 0.545$ Å, and $r_{Ni(LS)} = 0.56$ Å. From the foregoing results, it can be inferred that the B^{3+} ions with the smallest ionic radius surround most of the impurity Ni^{3+} ions with the highest ionic radius.

The ^6Li MAS NMR spectra of the B-doped samples (Fig. 6) show a single resonance line at ca. -1.6 ppm as referred to aqueous 1 M LiCl and the corresponding spinning sidebands. These spectra are similar to that found for pure $LiCoO_2$ and evidence little interaction of the lithium nucleus with possible boron nuclei in the second coordination sphere. On the contrary, ^{11}B spectra (referred to borax) show a complex envelope that may be decomposed into one narrower and three broader Gaussian components (Fig. 7, Table 3). In addition, the contribution of unresolved low-intensity spinning sidebands to these profiles cannot be discarded under the experimental conditions used in the
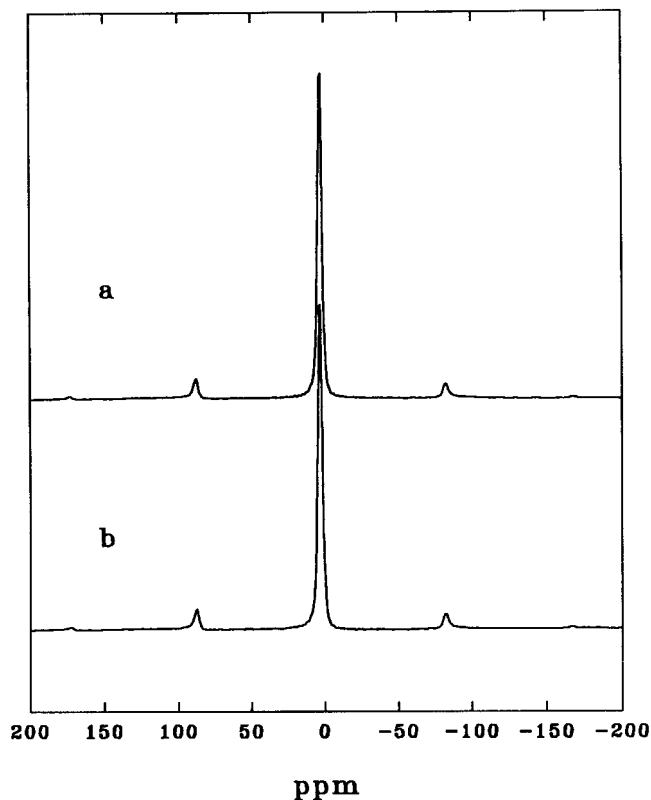
FIG 6. ^{6}Li MAS NMR spectra of B-doped samples: (a) 5 and (b) 20 atom %.

relatively large hyperfine shift constant (ca. 50 ppm) can be related with the interaction of the boron nucleus with Ni^{3+} ions in the neighbor coordination sphere. This suggestion agrees well with the EPR data on the distribution of Ni^{3+} impurities around the B^{3+} ions in the CoO_2 layers. Taking into account the connectivity of the O_4 pseudotetrahedra coordinating B with NiO_6 octahedra (Fig. 2), the hyperfine shift constant would comprise the direct transfer of spin density of Ni^{3+} ions toward the boron nucleus (at a distance of $1.19 \times a$), as well as the ca. $145°$ B(6c)–O–Ni(3a) indirect exchange.

It is interesting to compare the contribution of the Ni^{3+} ions to the chemical shifts of the boron and lithium nuclei. Recently, carrying out ^{6,7}Li MAS NMR investigations on $LiNi_{1-y}Co_yO_2$ solid solutions, Hirschinger $et\ al.$ (27) showed that the $90°$ Li–O–Ni and $180°$ Li–O–Ni couplings yield large positive and small negative hyperfine shift constants: $\sigma_{hf}^I = 113$ ppm and $\sigma_{hf}^{II} = -15$ ppm, respectively. Having in mind this angular dependence, it seems that the value of the hyperfine shift constant, attributed to $145°$ B–O–Ni coupling, is reasonable ($\sigma \cong 50$ ppm).

The main conclusion from the XRD, IR, EPR, and ^{11}B MAS NMR data is that, up to ca. 5 at.%, boron additives occupy the CoO_2 layers of trigonal $LiCoO_2$ in different sites than those of Co. The presence of boron perturbs the lattice dynamics. Since lattice dynamics has an important influence on lithium transport in the crystal framework, significant changes in the electrochemical properties of B-doped $LiCoO_2$ were found, as shown in the following.

As the addition of more than 5 at.% of B leads to an increasing amount of external borate compounds, a comparison of the electrochemical results was carried out between samples with 0 and 5% B. The results are summarized in Figs. 8 and 9 and Table 4. Figure 8 shows the SPES results (intensity vs. cell voltage and cell voltage vs. capacity) of the first charge–discharge cycle of lithium cells using the two oxide samples as active electrode material. In both samples, the charge branches show a main oxidation process at ca. 4 V. In previous studies, this effect was unambiguously assigned to the transition from $LiCoO_2$ to $Li_{0.8}CoO_2$, which is accompanied by an expansion of the c hexagonal lattice parameter (28, 29). The oxidation peak in the intensity profiles occurs at the voltage values collected in Table 4. The position of this peak for the B-doped sample is similar to that observed in the boron-free sample. The voltage values of both samples are higher than those usually observed for low-temperature $LiCoO_2$ (14, 15), giving additional evidence for the fact that the rhombohedral structure is preserved in B-doped samples. On the other hand, the main reduction peak observed during cell discharge is located at a higher voltage in the B-doped sample, consequently leading to a lower voltage difference between oxidation and reduction.
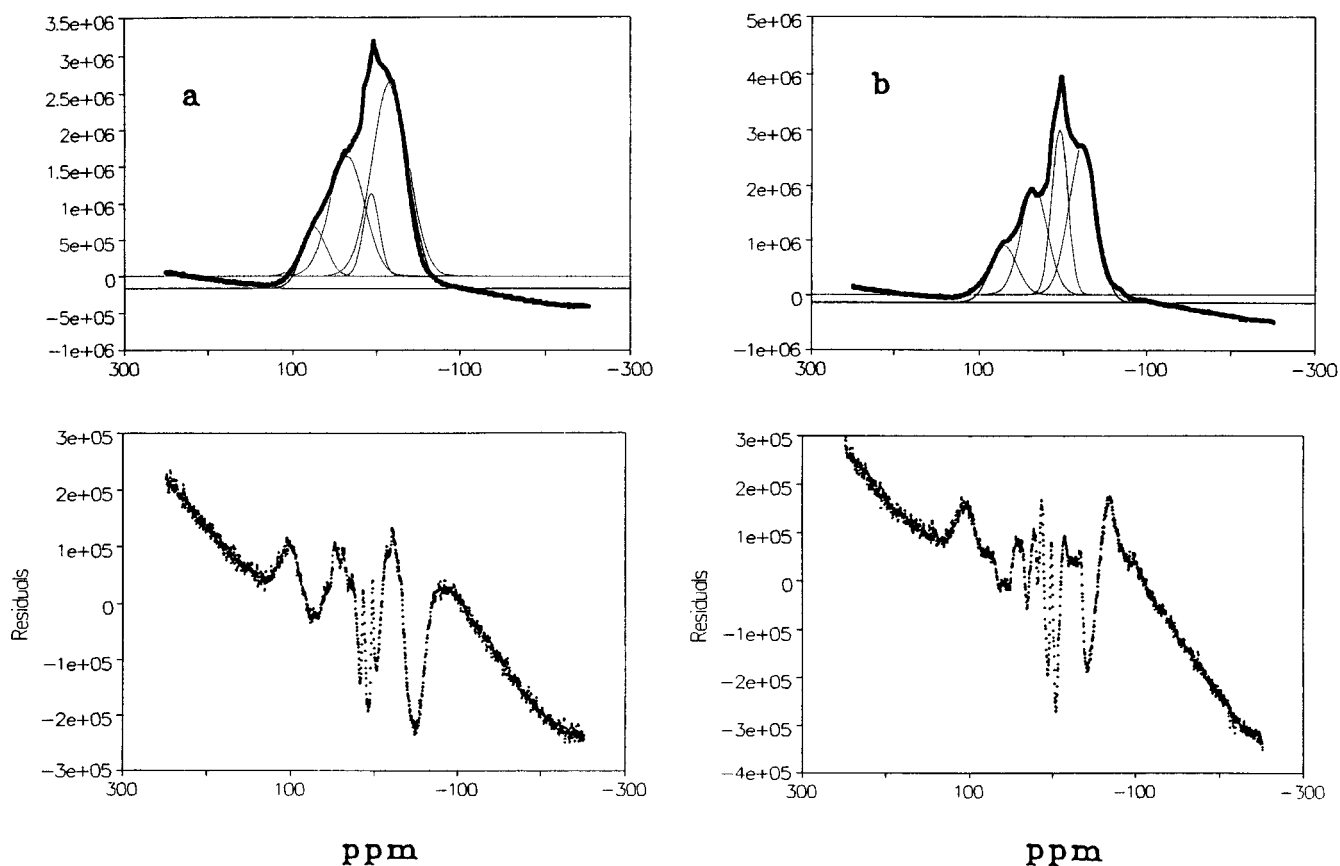
study. The narrower Gaussian (signal A) is centered at ca. 6 ppm and the difference in the positions between the three broader Gaussians (signals B, B′, and B″) is proportional to ca. 50 ppm. It is evident that signal A grows in intensity as the B content increases, while the ratio between the B, B′, and B″ signals is independent of the B content (Table 3). Hence, signal A can be assigned to boron in pyro- and/or metaborate salts, which appear for the sample with a higher B content, as detected by IR spectroscopy. In pyro- and metaborates it is known that boron is three-coordinated. Experimentally, it has been shown that the difference in chemical shift for three- and four-coordinated B is ca. 17 ppm in crystalline and vitreous boron oxides (24–26). The strong negative shift (23–27 ppm) of the principal resonance (signal B) toward signal A indicates an increased coordination number of boron. For B-doped $LiCoO_2$, this means that signal B corresponds most probably to four-coordinated boron; i.e., this signal can be attributed to the B atoms located in pseudotetrahedral sites of the CoO_2 layers (6c sites of the $R\bar{3}m$ space group with $z_B = 0.295$). The origin of the equidistant B′ and B″ signals (ca. 50 ppm apart from each other) is most probably due to the coupling between a nuclear moment of ^{11}B ($I = \frac{3}{2}$) and an electronic moment of one and two Ni^{3+} ions ($S = \frac{1}{2}$), respectively. The

FIG 7. ^{11}B MAS NMR spectra and profile fitting of B-doped samples: (a) 5 and (b) 20 atom %.

As usually found in nonequilibrium potentiostatic measurements, the voltage difference can be explained in terms of kinetic effects. Thus, boron additives in trigonal LiCoO$_2$ provide a better reversibility of the lithium intercalation–deintercalation process than in pure LiCoO$_2$. Additional evidence for the better reversibility of boron-doped LiCoO$_2$ comes from the lower peak intensity of the main reduction effect observed for the sample with 0.00% B and from the higher capacity of the first discharge for the doped sample (Table 4).

Between 4.1 and 4.2 V, two low-intensity oxidation peaks are clearly present in the B-doped sample but not in the nondoped LiCoO$_2$ sample. Only in the experiments where cell voltages higher than 4.4 V were reached during charge were these peaks hardly visible for the 0.00% B sample. However, in those experiments in which the upper limit of the potential window was increased, an enhanced discharge capacity loss was observed. Due to the use of two-electrode cells, the possible contribution of the anode to the occurrence of intensity peaks cannot be discarded. However, for high-purity LiCoO$_2$ electrodes, Dahn et al. (28, 29) ascribed two similar peaks to the formation of superlattice ordering of lithium ions at ca. $x = \frac{1}{2}$ in Li$_x$CoO$_2$ with a lattice distortion from hexagonal to monoclinic symmetry. Similarly, the presence of small amounts of nickel (2 atom %) in CoO$_2$ layers was shown to limit the occurrence of ordered phases (29). The presence of boron impurities seems to play the opposite role; i.e., boron dopants favor lattice adaptation to a superlattice structure of the Li ions. The different roles of nickel and boron may be related to different elastic
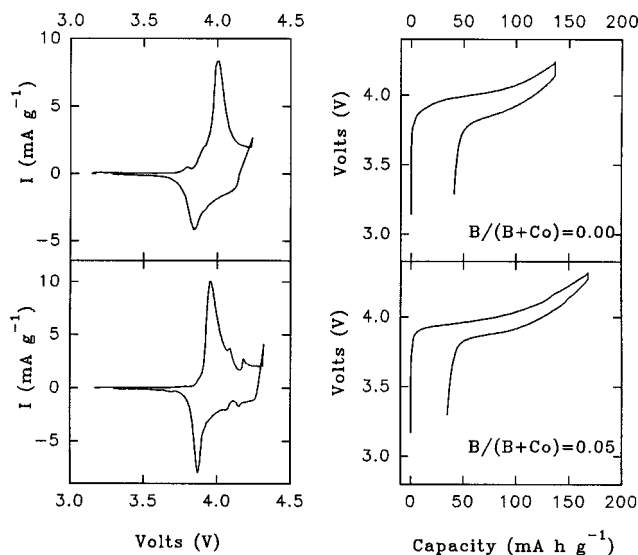
TABLE 3
Results of the Fitting of Four Gaussian Profiles to the Complex ^{11}B MAS NMR

B/(B+Co)	Peak	Amplitude/10^5	Center (ppm)	Width (ppm)	Area (%)
0.20	B	27.5	−22.0	39.0	38.1
	A	30.0	5.6	22.3	23.8
	B′	19.3	35.8	37.6	25.9
	B″	9.1	73.0	37.6	12.2
0.05	B	26.5	−16.0	51.2	51.1
	A	11.3	6.8	22.8	9.7
	B′	16.4	35.9	48.8	30.3
	B″	6.7	76.0	35.3	8.9

FIG 8. SPES results (intensity vs voltage and cell voltage vs capacity) of lithium cells using $LiCoO_2$ and the 5 atom % B-doped sample as positive electrode material.

properties of the $LiCoO_2$ matrix: nickel dopants in octahedral $3a$ sites increase the rigidity of the lattice and thus inhibit lithium ordering, whereas boron dopants in pseudotetrahedral $6c$ sites make the structure more flexible with respect to lithium ordering. Moreover, it should be noted that whereas impurity nickel ions have a tendency to occupy
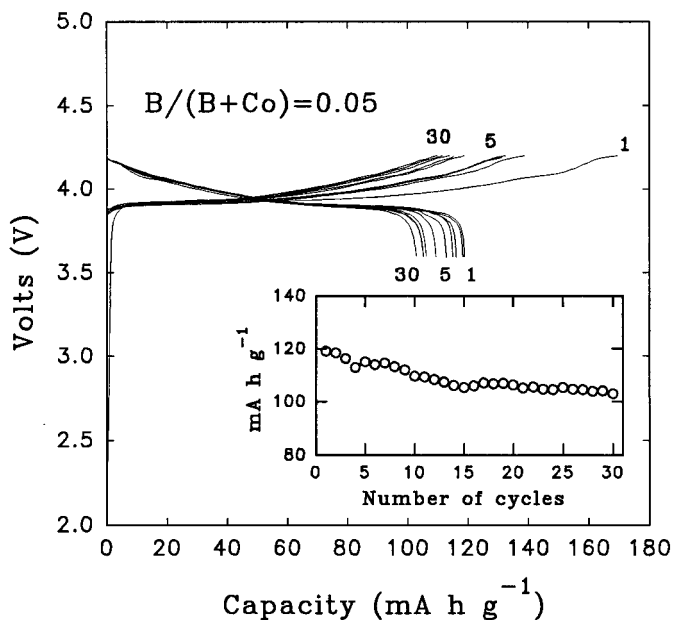

FIG 9. Galvanostatic cycling of lithium cells using the 5 atom % B-doped $LiCoO_2$ sample as the positive electrode active material, recorded at $C/100$.

TABLE 4
Results of Potentiostatic and Galvanostatic Experiments of Lithium Cells

B/(B + Co)	V_{oxid}	V_{red}	ΔV	$Q_p^{1st\ cycle}$	$Q_g^{1st\ cycle}$	$Q_g^{4th\ cycle}$
0.00	4.01	3.84	0.17	96	86	74
0.05	3.96	3.87	0.09	134	119	113

Note. V_{oxid}, Position of the main oxidation peak (volts) in potentiostatic mode, V_{red}, position of the main reduction peak (volts) in potentiostatic mode, ΔV, $V_{oxid} - V_{red}$, Q_p, cell capacity (mA h g^{-1}) in potentiostatic mode recorded at 10 mV h^{-1}, Q_g, Cell capacity (mA h g^{-1}) in galvanostatic mode recorded at $C/100$.

interlayer sites, boron may displace the trace impurity Ni atoms always present in "pure" $LiCoO_2$ to regular $3a$ sites within the CoO_2 layers. A similar behavior was observed in Ge-doped $LiCoO_2$. When the germanium dopant content was increased, the relative amount of Ni^{3+} ions in regular crystal sites increased (30).

Finally, Table 4 compares the capacity values obtained in potentiostatic and galvanostatic experiments for the two $LiCoO_2$ samples prepared under the same experimental conditions without boron and with 5 at.% B. For the first cycle recorded under both modes, the boron-free sample displays a lower capacity than that provided by the B-doped sample. Moreover, a less pronounced decrease in voltage at the end of the fourth galvanostatic discharge is observed for the boron-containing material. The good cycling behavior for $B/(B + Co) = 0.05$ is particularly evident from the shape of the successive galvanostatic cycles shown in Fig. 9. The charge branches are almost coincident for all cycles, which is consistent with the modified elastic properties of the layered solid which avoid the damage of the structure. The galvanostatic plots of the B-doped sample in Fig. 9 also show a significant change in the slope of the charge curves at ca. 4.1–4.2 V which is not seen for B-free $LiCoO_2$. This effect is consistent with the lithium ordering intensity peaks observed by SPES (Fig. 8), which emphasize lattice adaptability in B-doped $LiCoO_2$.

CONCLUSIONS

Up to 5 at.%, boron dopants occupy lattice sites different from those occupied by Li and Co atoms in trigonal $LiCoO_2$. The boron-doped samples show a displacement of the main reduction peak toward higher voltages, which is accompanied by a decrease in the voltage difference between oxidation and reduction. The improvement in the reversibility of the lithium deintercalation–intercalation process favors lattice adaptation to a superlattice structure of the lithium ions. A higher capacity of the first discharge and a significant improvement in capacity retention are also observed for B-doped samples.

REFERENCES

1. W. D. Johnston, R. P. Heikes, and D. Sestrich, *J. Phys. Chem. Solids* **7,** 1 (1958).
2. H. J. Orman and P. J. Wiseman, *Acta Crystallogr. C* **40,** 12 (1984).
3. T. Nagaura, M. Nagamine, I. Tanabe, and N. Miyamoto, *Prog. Batt. Solar Cells* **8,** 84 (1989).
4. T. Nagaura and T. Tozawa, *Prog. Batteries. Sol. Cells* **9,** 20 (1990).
5. K. Ozawa, *Solid State Ionics* **69,** 212 (1994).
6. C. Delmas and I. Saadoune, *Solid State Ionics* **53–56,** 370 (1992).
7. T. Ohzuku, K. Sawai, A. Ueda, M. Nagayama, Y. Iwakoshi, and H. Komori, *Electrochim. Acta* **38,** 1159 (1993).
8. A. Ueda and T. Ohzuku, *J. Electrochem. Soc.* **141,** 2010 (1994).
9. J. Morales, R. Stoyanova, J. L. Tirado, and E. Zhecheva, *J. Solid State Chem.* **113,** 182 (1994).
10. R. Stoyanova, E. Zhecheva, and L. Zarkova, *Solid State Ionics* **73,** 233 (1994).
11. C. D. W. Jones, E. Rossen, and J. R. Dahn, *Solid State Ionics* **68,** 65 (1994).
12. Y. Toyoguchi, European patent application 90106149.9, 1990. [filed Mar 30, 1990, published Oct 10, 1990].
13. M. Mizutani and T. Fukunaga, Jpn. Kokai Tokyo Koho JP 05,325,971 (93,325,971) (Cl. H01M4/58), Dec 10, 1993. M. Mizutani and T. Fukunaga, JP Appl. 92/47,942, Feb 3, 1992. [9 pages]
14. R. J. Gummow, M. M. Thackeray, W. I. F. David, and S. Hull, *Mater. Res. Bull.* **27,** 327 (1992).
15. R. J. Gummow, D. C. Liles, M. M. Thackeray, and W. I. F. David, *Mater. Res. Bull.* **28,** 1177 (1993).
16. E. Rossen, J. N. Reimers, and J. R. Dahn, *Solid State Ionics* **62,** 53 (1993).
17. R. J. Gummow and M. M. Thackeray, *J. Electrochem. Soc.* **140,** 3365 (1993).
18. R. K. Moore and W. B. White, *J. Am. Ceram. Soc.* **53,** 679 (1970).
19. P. Tarte and J. Preudhomme, *Spectrochim. Acta A* **26,** 747 (1970).
20. E. I. Kamitos, A. P. Patsis, M. A. Karakassides, and G. D. Chryssikos, *J. Non-Cryst. Solids* **126,** 52 (1990).
21. A. Rulmont and M. Almou, *Spectrochim. Acta A* **45,** 603 (1989).
22. S. Angelov, C. Friebel, E. Zhecheva, and R. Stoyanova, *J. Phys. Chem. Solids* **53,** 443 (1992).
23. J. H. Van Vleck, *Phys. Rev.* **73,** 1249 (1948).
24. G. L. Turner, K. A. Smith, R. J. Kirpatrick, and E. Oldfield, *J. Magn. Reson.* **67,** 544 (1986).
25. L. van Wielen and W. Müller-Warmuth, *Solid State Nucl. Magn. Reson.* **2,** 279 (1993).
26. J.A. Tussell, *J. Non-Cryst. Solids* **185,** 307 (1995).
27. C. Marichal, J. Hirschinger, P. Granger, M. Ménétrier, A. Rougier, and C. Delmas, *Inorg. Chem.* **34,** 1773 (1995).
28. J. N. Reimers and J. R. Dahn, *J. Electrochem. Soc.* **139,** 2091 (1992).
29. J. N. Reimers, J. R. Dahn, and U. von Sacken, *J. Electrochem. Soc.* **140,** 2752 (1993).
30. J. P. Kemp and P. A. Cox, *J. Phys. Chem. Solids* **51,** 575 (1990).